

Numerical Heat Transfer, Part B: Fundamentals



ISSN: 1040-7790 (Print) 1521-0626 (Online) Journal homepage: http://www.tandfonline.com/loi/unhb20

Numerical Prediction of Dispersion and Evaporation of Liquid Sprays in Gases Flowing at all Speeds

F. Moukalled & M. Darwish

To cite this article: F. Moukalled & M. Darwish (2008) Numerical Prediction of Dispersion and Evaporation of Liquid Sprays in Gases Flowing at all Speeds, Numerical Heat Transfer, Part B: Fundamentals, 54:3, 185-212, DOI: 10.1080/10407790802182679

To link to this article: http://dx.doi.org/10.1080/10407790802182679

	Published online: 29 Jul 2008.
	Submit your article to this journal $oldsymbol{oldsymbol{\mathcal{G}}}$
hil	Article views: 96
Q ^L	View related articles 🗗
2	Citing articles: 2 View citing articles 🗹

Full Terms & Conditions of access and use can be found at http://www.tandfonline.com/action/journalInformation?journalCode=unhb20

Copyright © Taylor & Francis Group, LLC ISSN: 1040-7790 print/1521-0626 online

DOI: 10.1080/10407790802182679



NUMERICAL PREDICTION OF DISPERSION AND EVAPORATION OF LIQUID SPRAYS IN GASES FLOWING AT ALL SPEEDS

F. Moukalled and M. Darwish

Faculty of Engineering and Architecture, Mechanical Engineering Department, American University of Beirut, Beirut, Lebanon

This work is concerned with the formulation, implementation, and testing of an all-speed numerical procedure for the simulation of turbulent dispersion and evaporation of droplets. The pressure-based method is formulated, for both the discrete and continuous phases, within a Eulerian framework following a finite-volume approach and is equally applicable in the subsonic and supersonic regimes. The two-equation $k-\epsilon$ turbulence model is used to estimate turbulence in the gas phase with modifications to account for compressibility at high speeds, while an algebraic model is employed to predict turbulence in the discrete phase. Two configurations involving streamwise and cross-stream injection are investigated, and solutions for evaporation and mixing of droplets sprayed into subsonic and supersonic streams are generated over a wide range of operating conditions. Results, displayed in the form of velocity vector fields and contour plots, reveal the degree of penetration of the injected droplet into the gas phase, and the rate of evaporation as a function of inlet gas temperature, inlet droplet temperature, and/or length of the domain.

INTRODUCTION

Recently there has been a revived interest in the injection of liquids in supersonic streams, particularly with respect to fuel injection techniques for hypersonic flights. These designs require air-breathing engines capable of supersonic combustion. The scramjet (supersonic combustion ramjet) appears at present to be a practical engine for these types of applications. Its concept is fairly old, and was the subject of studies throughout the 1960s and again in the 1980s. However, its coming to fruition depends on, among other things, the development of numerical tools for the simulation of its supersonic combustion process and related phenomena. More specifically, effective penetration and enhanced mixing of hydrocarbon fuels in a gas flowing at supersonic speed are crucial ingredients for the success of any scramjet design [1]. Three key issues govern the performance of the liquid injection process in the scramjet engine: the penetration of the fuel into the free stream, the atomization

Received 2 November 2007; accepted 30 April 2008.

The support provided by the Lebanese National Council for Scientific Research (LNCSR) through Grants 113040-022142 and 022129 is gratefully acknowledged.

Address correspondence to F. Moukalled, Mechanical Engineering Department, Faculty of Engineering and Architecture, American University of Beirut, P.O. Box 11-0236, Riad El Solh, Beirut, 1107 2020, Lebanon. E-mail: memouk@aub.edu.lb

NOMENCLATURE				
$A_P^{(k)}, \dots$	coefficients in the discretized	Sc	Schmidt number	
(1)	equation for $\phi^{(k)}$	t	time	
$B_P^{(k)}$	source term in the discretized	T	temperature of fluid/phase k	
	equation for $\phi^{(k)}$	u, v	velocity components in x and y	
C_P	specific heat at constant pressure		directions, respectively	
$egin{array}{c} C_D \ C_{ ho}^{(k)} \end{array}$	drag coefficient	U_f	interface flux velocity $(\mathbf{v}_f^{(k)} \cdot \mathbf{S}_f)$	
$C_{ ho}^{(\kappa)}$	coefficient equals to	v	velocity vector	
	$1/R^{(k)}T^{(k)}$	Y	vapor mass fraction	
d_{α}	droplet diameter	α	volume fraction	
$\mathbf{D}_P^{(k)}[\mathbf{\phi}^{(k)}]$	the matrix D operator	$\beta_{(k)}$	thermal expansion coefficient for	
\mathbf{F}_{p}^{B}	body force		phase/fluid k	
\mathbf{F}^D	drag force	Γ	diffusion coefficient	
h	static enthalpy	δt	time step	
$h_{\mathrm{cor},d}$	correction coefficient for heat	Δh_{v}	latent heat	
	transport in droplet evaporation	3	turbulence dissipation rate	
	model	η	Kolmogorov microscale	
H	total enthalpy	λ	conductivity coefficient	
$H_P[\phi^{(k)}]$	the H operator	$\mu, \mu_t, \mu_{\text{eff}}$	laminar, turbulent, and effective	
$\mathbf{H}_{P}[\mathbf{u}^{(k)}]$	the vector form of the H		viscosities of fluid/phase k	
	operator	ρ	density	
k	turbulence kinetic energy	τ	the stress tensor	
$m_{\mathrm{cor},d}$	correction coefficient for mass	ф	general scalar quantity	
	transport in droplet evaporation	Ω	cell volume	
	model	Subscripts		
\dot{m}_d	mass rate of droplet evaporation	d	refers to the droplet phase	
M_d	volumetric mass rate of droplet	eff	refers to effective values	
	evaporation	f	refers to interface	
p	pressure	g	refers to the gas phase	
P_k	production term in k and ϵ	i	refers to size group <i>i</i>	
D.,	equations	k	refers to phase k	
Pr	laminar Prandtl number of	nb	refers to the east, west,, face of	
D _m	fluid/phase k		a control volume	
Pr_t	turbulent Prandtl number of	NB	refers to the East, West,,	
	fluid/phase k general source term of		neighbors of the main grid point	
$Q_{(k)}$	general source term of fluid/phase k	P	refers to the P grid point	
P	gas constant for fluid/phase k	S	refers to the droplet surface	
$R_{(k)}$	Reynolds number based on the		condition	
IX.C	droplet diameter	sat	refers to the saturation condition	
S	source term	vap, g	refers to the vapor species in the	
\mathbf{S}_f	surface vector		gas phase	
i g _f	surface vector			

of the injected fuel drops, and the level of fuel/air mixing [2]. It is important for the fuel to penetrate effectively into the free stream so that the combustion process produces an even temperature distribution; otherwise it will mostly occur along the surface of the combustor, causing inefficient combustor operation and increased cooling problems. Rapid atomization of the fuel is also required for efficient combustion, as it results in increased fuel/air mixing, allowing a higher percentage of the fuel to be burned in the short time before the entire mixture passes out of the combustor

(generally, the flow residence time is of the order of a few milliseconds [3]). This article is aimed at developing a numerical method capable of predicting the spreading and evaporation of liquid droplets injected in gases flowing at all speeds.

The complex multiphase flow phenomena governing liquid injection applications involve a continuous gas phase usually composed of air and the evaporating vapor species and one or more dispersed liquid phases, each composed of either a single component or a multicomponent fuel. In the case of a single-component fuel, the evaporation rate of the droplet will be uniform, since only one species of spatially uniform properties is present. It should be noted, however, that it is possible to have several evaporating but chemically distinct species evaporating, i.e., several kinds of single-component fuel droplet evaporating, where each is treated as a separate fluid interacting with the gas phase. Moreover, each type will have its own evaporation rate. On the other hand, a multicomponent fuel [4] consists of a blend of several species of hydrocarbons contained in the same droplet. These hydrocarbons generally have different volatilities, and the high-volatility components will evaporate early in the process while the lower-volatility components will be retained until later in the process. Thus the molar weight of the multicomponent fuel will vary during evaporation, which will affect all thermophysical properties of the fuel. Singlecomponent fuel is of interest in this work.

Approaches for the simulation of droplet transport and evaporation in combustion systems can be classified under two categories, the Lagrangian and Eulerian methods. In both techniques, the gaseous phase is calculated by solving the Navier-Stokes equations with a standard discretization method such as the finite-volume method.

In the Lagrangian approach [5–7], the spray is represented by discrete droplets, which are advected explicitly through the computational domain while accounting for evaporation and other phenomena. Due to the large number of droplets in a spray, each discrete computational droplet is made to represent a number of physical droplets averaging their characteristics. The equations of motion of each droplet are a set of ordinary differential equations (ODE) which are solved using an ODE solver, a numerical procedure different from that of the continuous phase. To account for the interaction between the gaseous phase and the spray, several iterations of alternating solutions of the gaseous phase and the spray have to be conducted.

In the Eulerian approach [6–9], the evaporating spray is treated as an interacting and interpenetrating continuum. In analogy to the continuum approach of single-phase flows, each phase is described by a set of transport equations for mass, momentum, and energy extended by interfacial exchange terms. This description allows the gaseous phase and the spray to be discretized by the same method, and therefore to be solved by the same numerical procedure. Because of the presence of multiple phases, a multiphase algorithm is used.

Several investigations dealing with spray modeling have been reported. Nmira et al. [10] used a Eulerian-Eulerian two-phase approach to study thermoplastic fire suppression by water sprays. Raju [11] employed the Monte Carlo probability density function method to model turbulent spray flames on unstructured grids. Chow [12] studied numerically the interaction of a water spray with a smoke by subdividing the spray into several classes based on the droplet distribution function.

Tolpadi et al. [13] developed a quasi-steady droplet vaporization model in which droplet heating and vaporization take place simultaneously. Kim et al. [14] employed a Eulerian-Lagrangian approach to study the initiation and propagation of detonation waves in an air—fuel spray mixture. Raju [15] integrated the Monte Carlo probability density function, a Lagrangian-based dilute spray model, and an Eulerian solver to model turbulent spray flames using parallel computing. Liu and Reitz [16] developed a mixed laminar and turbulent model of heat transfer for describing impinging fuel sprays in direct injection diesel engines. Chen and Pereira [17] used a Eulerian-Lagrangian stochastic model to investigate a confined evaporating isopropyl alcohol spray issuing into a co-flowing, heated turbulent air stream. Jicha et al. [18] adopted a Eulerian-Lagragian approach to study a turbulent gas—liquid droplet flow in a two-dimensional plane channel.

In this work, a numerical method for the simulation of droplet evaporation and scattering in a stream flowing at any speed is developed. This is achieved through a multifluid, all-speed, pressure-based finite-volume flow solver in which a droplet evaporation model is implemented. The model as it stands does not take into considerations droplet breakup or coalescence, but different droplet sizes are accounted for. The use of a Eulerian approach has many advantages: the same validated numerical procedure used for all phases, ease of implementation of acceleration techniques (such as multigrid), and improvements to code can be carried over to all phases.

In the remainder of this article, the governing equations for droplet transport and evaporation are first presented, followed by a brief description of the discretization method and solution procedure. Then, results obtained for two physical configurations are discussed.

THE GOVERNING EQUATIONS

The conservation equations needed to solve for the interacting flows of interest can best be understood by referring to Figure 1a. A gas moving at subsonic/supersonic speed enters a domain with liquid droplets being injected into the gas while flowing. The droplets move with the gas, evaporate, and decrease in size. The equations required to solve for this multiphase flow are those representing the conservation of mass, momentum, and energy for both the gas and droplet phases. Moreover, equations to track the mass fraction of the evaporating liquid in the gas phase and to compute the size of the droplets for each droplet phase are needed. Furthermore, for turbulent flows, additional equations to compute the turbulent viscosity or Reynolds stresses are necessary. The number of these equations depends on the turbulence model used. In this work the standard $k-\varepsilon$ model [19, 20] is employed for the gaseous phase, while an algebraic model based on a Boussinesq approach [8] approximates the turbulence terms in the droplet-phase transport equations. Neglecting interaction between droplets, the flow fields are described by the transport equations presented next.

Droplet Evaporation Model

Evaporation is accounted for in the various conservation equations via source terms that are derived following the uniform temperature model [21–23]. This

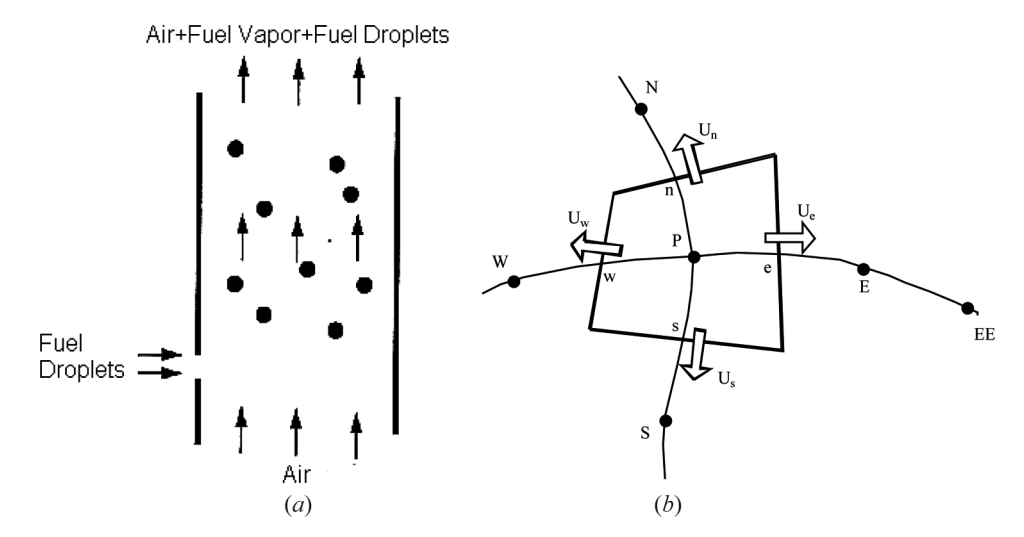


Figure 1. (a) A schematic depiction of the physical situation considered. (b) Control volume.

computationally effective droplet model is based on the assumption of a homogeneous internal temperature distribution in the droplet and phase equilibrium conditions at the surface. The analytical derivation of this model does not consider contributions to heat and mass transport through forced convection by the gas flow around the droplet. Forced convection is taken into account by means of two empirical correction factors, $m_{\text{cor},d}^{(k)}$ and $h_{\text{cor},d}^{(k)}$ [24, 25]. The evaporation rate from a droplet is commonly expressed as

$$\frac{dm_d}{dt} = \dot{m}_d^* \tag{1}$$

where m_d is the mass of the liquid droplet and \dot{m}_d^* is the mass flux, corrected using the Frössling correlation and based on the classical droplet vaporization model [24, 25]. Using reference values for variable fluid properties based on the 1/3 rule of Sparrow and Gregg [26], an integration of the radially symmetric differential equations yields an expression for the transport fluxes, which is given by

$$\dot{m}_d^* = m_{\text{cor},d}\dot{m}_d = m_{\text{cor},d} \left[-2\pi d_d \rho_{g,\text{ref}} \Gamma_{dg,\text{ref}} \ln \left(\frac{1 - Y_{\text{vap},g,\infty}}{1 - Y_{\text{vap},g,s}} \right) \right]$$
(2)

In Eq. (2) and the equations to follow, the subscript "ref" indicates that the variable is evaluated at the reference temperature and mass fraction, which are defined as

$$T_{\text{ref}} = \frac{1}{3} T_{\text{vap},g,\infty} + \frac{2}{3} T_{\text{vap},g,s}$$
 $Y_{\text{ref}} = \frac{1}{3} Y_{\text{vap},g,\infty} + \frac{2}{3} Y_{\text{vap},g,s}$ (3)

where $T_{\mathrm{vap},g,s}$ and $Y_{\mathrm{vap},g,s}$ are the temperature and mass fraction of the vapor at the surface of the droplet. Thus $\rho_{g,\mathrm{ref}}$ and $\Gamma_{d-g,\mathrm{ref}}$ are the gas density and vapor diffusion coefficient evaluated at the reference temperature and mass fraction. Since the

uniform temperature model [21–23] is used, the temperature at the droplet surface is basically equal to that of the droplet (i.e., $T_{\text{vap},g,s} = T_d$).

On the other hand, the vapor concentration on the surface of the droplet is found using the exponential law of Cox-Antoine [21] as

$$X_{\text{vap,g,s}}(p_{\text{sat}}) = \frac{p_{\text{sat}}}{p} \tag{4}$$

with the saturation pressure p_{sat} for a droplet at temperature T_d obtained from

$$P_{\text{sat}}(T_d) = e^{A+B/(T_d+C)} \tag{5}$$

where A, B, and C are specific values for the liquid under consideration. Thus

$$Y_{\text{vap,s}} = \frac{X_{\text{vap,g,s}} \text{MW}_{\text{vap}}}{X_{\text{vap,g,s}} \text{MW}_{\text{vap}} + (1 - X_{\text{vap,g,s}}) \text{MW}_{\text{air}}}$$
(6)

where MW is the molecular weight.

The droplet temperature increases due to heat transfer from the hotter gas phase. Once enough energy has been transferred to overcome the latent heat of evaporation, evaporation is initiated. This can be expressed mathematically as

$$h_{\text{vap},g,s} - h_{d,s} = \Delta h_{\text{vap}}(T_{d,s}) \tag{7}$$

The heat balance equation for the droplet can be written as

$$m_d \frac{d(c_p T_d)}{dt} = \dot{Q}_{\text{evap},s} + \dot{Q}_{\text{conv},s}$$
 (8)

where h_d is the static enthalpy and $\dot{Q}_{\text{conv},s}$ and $\dot{Q}_{\text{evap},s}$ are the convection and evaporation heat transfer rates, respectively, given by

$$\dot{Q}_{\text{conv},s} = \pi d_d^2 \beta_d^* (T_{g,s} - T_d) \tag{9}$$

where β_d^* is the corrected convective heat transfer coefficient given by

$$\beta_d^* = h_{\text{cor},d} \frac{-\dot{m}_d c_{p,\text{vap,ref},d} / \pi d_d^2}{\exp(-\dot{m}_d c_{p,\text{vap,ref},d} / 2\pi d_d \lambda_{g,\text{ref}}) - 1}$$
(10)

and

$$\dot{Q}_{\text{evap},s} = \dot{m}_d^* \, \Delta h_v \tag{11}$$

The correction factors $m_{\text{cor},d}$ and $h_{\text{cor},d}$ account for convective mass and heat transport and are computed from [24, 25]

$$m_{\text{cor},d} = 1 + 0.276 \,\text{Re}^{1/2} \,\text{Sc}^{1/3} \qquad h_{\text{cor},d} = 1 + 0.276 \,\text{Re}^{1/2} \,\text{Pr}^{1/3}$$
 (12)

where Re, Sc, and Pr are the Reynolds, Schmidt, and Prandtl numbers, respectively, defined as

$$Re = \frac{\rho_g \|\mathbf{v}_d - \mathbf{v}_g\| d_d}{\mu_{e,ref}} \qquad Sc = \frac{\mu_{g,ref}}{\rho_{e,ref} \Gamma_{dg,ref}} \qquad Pr = \frac{\mu_{g,ref} c_{p,g,ref}}{\lambda_{g,ref}}$$
(13)

From the above, it follows that the energy equation for the droplet can be written as

$$\frac{d(m_d h_d)}{dt} = \dot{m}_d^* (\Delta h_v + h_d) + \pi d_d^2 \beta_d^* (T_d - T_g)$$
 (14)

The right-hand sides of Eqs. (2) and (14) represent the mass and energy sources due to evaporation from the droplet.

Gas Balance Equations

The continuity, momentum, energy, turbulence kinetic energy, and turbulence dissipation rate equations for the gas phase, which is composed of two species, air and vapor, in addition to the mass fraction equation of the fuel vapor in the gaseous phase, are given by

$$\frac{\partial}{\partial t}(\alpha_g \rho_g) + \nabla \cdot (\alpha_g \rho_g \mathbf{v}_g) = \nabla \cdot \left(\frac{\mu_{t,g}}{\mathrm{Sc}_{t,g}} \nabla \alpha_g\right) - \sum_{k \neq \sigma} \dot{\mathbf{M}}_d^{(k)}$$
(15)

$$\frac{\partial}{\partial t}(\alpha_g \rho_g \mathbf{v}_g) + \nabla \cdot (\alpha_g \rho_g \mathbf{v}_g \mathbf{v}_g) = -\alpha_g \nabla p + \nabla \cdot \overline{\overline{\tau}_g} + \mathbf{F}_g^B + \mathbf{F}_g^D - \sum_{k \neq g} \dot{\mathbf{M}}_d^{(k)} \mathbf{v}_d^{(k)}$$
(16)

$$\frac{\partial}{\partial t}(\alpha_g \rho_g k_g) + \nabla \cdot (\alpha_g \rho_g \mathbf{v}_g k_g) = \nabla \cdot (\alpha_g \mu_{\text{eff},g} \nabla k_g) + \alpha_g (P_k - \rho_g \varepsilon_g) + \mathbf{S}_{k,d}$$
(17)

$$\frac{\partial}{\partial t}(\alpha_{g}\rho_{g}\varepsilon_{g}) + \nabla \cdot (\alpha_{g}\rho_{g}\mathbf{v}_{g}\varepsilon_{g}) = \nabla \cdot (\alpha_{g}\mu_{\text{eff},\varepsilon,g}\nabla\varepsilon_{g}) + \alpha_{g}\left(C_{\varepsilon 1}\frac{\varepsilon_{g}}{k_{g}}P_{k} - C_{\varepsilon 2}\rho_{g}\frac{\varepsilon_{g}^{2}}{k_{g}}\right) + S_{\varepsilon,d}$$
(18)

$$\frac{\partial}{\partial t} (\alpha_g \rho_g H_g) + \nabla \cdot (\alpha_g \rho_g \mathbf{v}_g H_g) = \nabla \cdot (\alpha_g \lambda_g \nabla T_g) + \nabla \cdot \left(\alpha_g \frac{\mu_{t,g}}{\Pr_t} \nabla h_g \right)
+ \alpha_g \rho_g \mathbf{g} \cdot \mathbf{v}_g + \frac{\partial}{\partial t} (\alpha_g p) + \nabla \cdot (\alpha_g \mathbf{v}_g \overline{\tau}_g + \mu_{t,g} \nabla k_g)
+ \sum_{k \neq g} \pi (d_d^{(k)})^2 (\beta_d^{(k)})^* (T_d^{(k)} - T_g) - \sum_{k \neq g} \dot{\mathbf{M}}_d^{(k)} (\Delta h_{v,d}^{(k)} + h_d^{(k)})$$
(19)

$$\frac{\partial}{\partial t} (\alpha_g \rho_g Y_{\text{vap},g}) + \nabla \cdot (\alpha_g \rho_g \mathbf{v}_g Y_{\text{vap},g}) = \nabla \cdot (\alpha_g \Gamma_{\text{eff}} \nabla Y_{\text{vap},g}) - (1 - Y_{\text{vap},g}) \sum_{k \neq g} \dot{\mathbf{M}}_d^{(k)}$$
(20)

The evaporated liquid $\dot{M}_d^{(k)}$ appearing in the above equations is calculated from $(\dot{m}_d^{(k)})^*$, given by Eq. (2), as

$$\sum_{k \neq g} \dot{\mathbf{M}}_d^{(k)} = -\dot{\mathbf{M}}_{\text{vap},g} = \sum_{k \neq g} \frac{6\alpha_d^{(k)}}{\pi (d_d^{(k)})^3} (\dot{\mathbf{m}}_d^{(k)})^*$$
 (21)

Further, the terms \mathbf{F}_g^B and \mathbf{F}_g^D in Eq. (16) represent the body and drag forces, respectively. For the gas phase, the body force $(\mathbf{F}_g^B = \alpha_g \rho_g \mathbf{g})$ can be neglected; while the drag force due to liquid droplets is written as

$$F_g^D = -\sum_{k \neq g} \frac{3}{4} \alpha^{(k)} \rho_g \frac{C_D^{(k)}}{d_d^{(k)}} \| \mathbf{v}_d^{(k)} - \mathbf{v}_g \| (\mathbf{v}_g - \mathbf{v}_d^{(k)})$$
 (22)

where $d_d^{(k)}$ is the droplet diameter of the kth phase and the aerodynamic drag coefficient is given by [24]

$$C_D^{(k)} = 0.36 + \frac{24}{\text{Re}^{(k)}} + \frac{5.48}{[\text{Re}^{(k)}]^{0.573}}$$
 (23)

In Eqs. (16) and (19), $\overline{\tau_g}$ is the stress tensor given by

$$\overline{\overline{\tau_g}} = \alpha_g \mu_{\text{eff}} \left(\nabla \mathbf{v}_g + \nabla \mathbf{v}_g^T - \frac{2}{3} (\nabla \cdot \mathbf{v}_g) \mathbf{I} \right) \qquad \text{where } \mu_{\text{eff}} = \mu_g + \mu_{t,g}$$
 (24)

The total enthalpy H_g in the energy equation is given in terms of the static enthalpy h_g by

$$H_g = h_g + \frac{1}{2} \mathbf{v}_g \cdot \mathbf{v}_g + k_g$$
 where $h_g = Y_{\text{air}} h_{\text{air},g} + Y_{\text{vap}} h_{\text{vap},g}$ (25)

In addition, the two terms on the left-hand side of the energy equation [Eq. (19)] describe the rate of increase of H_g and the rate at which H_g is transported into and out of the control volume by convection. Further, the terms on the right-hand side of Eq. (19) represent, respectively, the rate of energy transfer into the control volume by conduction, the turbulent flux, the rate of work done by body forces, the pressure work, the viscous work, the heat transfer by convection between the liquid at temperature from $T_d^{(k)}$ and the gas at temperature T_g , and the heat added to the gas phase due to evaporation of the liquid droplets.

Moreover α_g , \mathbf{v}_g , and ρ_g are, respectively, the volume fraction, velocity, and density of the gas phase. The gas density may either be computed from the air and vapor densities or the ideal gas relation as

$$\frac{1}{\rho_g} = \frac{Y^{(\text{air})}}{\rho^{(\text{air})}} + \frac{Y^{(\text{vap})}}{\rho^{(\text{vap})}} \quad \text{or} \quad \rho_g = \frac{p}{R_g T_g} = \frac{p}{R_0 \left[\left(Y^{(\text{air})} / \text{MW}^{(\text{air})} \right) + \left(Y^{(\text{vap})} / \text{MW}^{(\text{vapor})} \right) \right] T_g}$$

$$(26)$$

where Y and ρ represent the mass fraction and density, R_g is the gas constant, and R_0 is the universal gas constant.

Droplet Balance Equations

The mass, momentum, droplet diameter, and energy conservation equations for a droplet phase are given by

$$\frac{\hat{\sigma}}{\hat{\sigma}_t}(\alpha_d^{(k)}\rho_d^{(k)}) + \nabla \cdot (\alpha_d^{(k)}\mathbf{v}_d^{(k)}\rho_d^{(k)}) = \nabla \cdot \left(\frac{\mu_{\text{turb},d}^{(k)}}{\mathbf{S}\mathbf{c}_{\text{turb},d}^{(k)}}\nabla \alpha_d^{(k)}\right) + \dot{\mathbf{M}}_d^{(k)}$$
(27)

$$\frac{\partial}{\partial t} (\alpha_d^{(k)} \rho_d^{(k)} \mathbf{v}_d^{(k)}) + \nabla \cdot (\alpha_d^{(k)} \rho_d^{(k)} \mathbf{v}_d^{(k)} \mathbf{v}_d^{(k)}) = -\alpha_d^{(k)} \nabla p + \mathbf{F}_d^{B,(k)} + \mathbf{F}_d^{D,(k)} + \dot{\mathbf{M}}_d^{(k)} \mathbf{v}_d^{(k)}$$
(28)

$$\frac{\partial}{\partial t} (\alpha_d^{(k)} \rho_d^{(k)} d_d^{(k)}) + \nabla \cdot (\alpha_d^{(k)} \rho_d^{(k)} \mathbf{v}_d^{(k)} d_d^{(k)}) = \nabla \cdot \left(\alpha_d^{(k)} \frac{\mu_{t,d}^{(k)}}{\Pr_{t,d}^{(k)}} \nabla d_d^{(k)} \right) + \frac{4}{3} d_d^{(k)} \dot{\mathbf{M}}_d^{(k)}$$
(29)

$$\frac{\partial}{\partial t} (\alpha_d^{(k)} \rho_d^{(k)} h_d^{(k)}) + \nabla \cdot (\alpha_d^{(k)} \rho_d^{(k)} \mathbf{v}_d^{(k)} h_d^{(k)}) = \nabla \cdot \left(\alpha_d^{(k)} \frac{\mu_{t,d}^{(k)}}{\Pr_{t,d}^{(k)}} \nabla h_d^{(k)} \right) + \alpha_d^{(k)} \rho_d^{(k)} \mathbf{g} \cdot \mathbf{v}_d^{(k)} + \pi (d_d^{(k)})^2 (\beta_d^{(k)})^* (T_g - T_d^{(k)}) + \dot{\mathbf{M}}_d^{(k)} (\Delta h_{v,d}^{(k)} + h_d^{(k)}) \tag{30}$$

The meaning of the various terms in the continuity, momentum, and energy equations of the droplet phase is as described for the gas-phase equations. The additional droplet diameter equation (29), which is derived from the mass conservation equation, is solved for every droplet phase to track the variation of the droplet diameter as evaporation occurs. The droplet diameter field is used to calculate the evaporation rate and the drag term. As mentioned earlier, droplet—droplet interactions through breakup and coalescence are not accounted for in this work, and only the liquid mass of each droplet size is transformed to vapor. This effect is currently under investigation and will form the subject of future studies.

In addition to the above equations, the volume fractions of the various phases have to satisfy a compatibility equation, which for an *n*-phase flow is given by

$$\sum_{k=1}^{n} \alpha^{(k)} = 1 \tag{31}$$

The turbulent viscosity of the disperse (droplet) phase, $\mu_{t,d}^{(k)}$, is modeled using the approach of Melville and Bray [27], according to which $\mu_{t,d}^{(k)}$ is given by

$$\mu_{t,d}^{(k)} = \mu_{t,g} \frac{\rho_d^{(k)}}{\rho_g} \frac{k_d^{(k)}}{k_g}$$
 (32)

The ratio of the turbulent kinetic energies of the kth dispersed (d) phase and gas (g) phase is calculated following the approach in [8, 28] as

$$\frac{k_d^{(k)}}{k_g} = \frac{1}{1 + (\omega_d^{(k)})^2 (\tau_d^{(k)})^2} \quad \text{where } k_d^{(k)} = \frac{1}{2} \mathbf{v}_d^{(k)} \cdot \mathbf{v}_d^{(k)}$$
 (33)

Since droplets do not generally follow the motion of the surrounding fluid from one point to another, the ratio $k_d^{(k)}/k_g$ is different from unity and varies with particle relaxation time t and local turbulence quantities. Krämer [28] recommends the following equation for the frequency of the particle response:

$$\omega_d^{(k)} = \frac{1}{\tau_d^{(k)}} \left(\frac{\sqrt{\frac{2}{3}} k_g}{L_x} \tau_d^{(k)} \right)^{1/4} \qquad \tau_d^{(k)} = \frac{1}{18} \frac{\rho_d^{(k)}}{\rho_g} \frac{(d_d^{(k)})^2}{\nu_g} \frac{1}{1 + 0.133 (\text{Re}_d^{(k)})^{0.687}}$$
(34)

with a characteristic macroscopic length scale of turbulence given by

$$L_{x} = (c_{\mu})^{3/4} \frac{(k_{g})^{3/2}}{\varepsilon_{p}}$$
 (35)

For the turbulent Schmidt number of the droplet phase, $Sc_{t,d}^{(k)}$, Krämer [28] suggests a value of 0.3. However, in a more recent work [8], it was found to be particle size-dependent, and a value of 0.7 is used in this work $(Sc_{t,d}^{(k)} = 0.7)$. For the turbulent Prandtl number, a value of 0.85 was chosen $(Pr_{t,d}^{(k)} = 0.85)$.

DISCRETIZATION PROCEDURE

A review of the above differential equations reveals that they are similar in structure. If a typical representative variable associated with phase (k) is denoted by $\phi^{(k)}$, the general fluidic differential equation may be written as

$$\frac{\partial(\boldsymbol{\alpha}^{(k)}\boldsymbol{\rho}^{(k)}\boldsymbol{\phi}^{(k)})}{\partial t} + \nabla \cdot (\boldsymbol{\alpha}^{(k)}\boldsymbol{\rho}^{(k)}\mathbf{u}^{(k)}\boldsymbol{\phi}^{(k)}) = \nabla \cdot (\boldsymbol{\alpha}^{(k)}\boldsymbol{\Gamma}^{(k)}\nabla\boldsymbol{\phi}^{(k)}) + \boldsymbol{\alpha}^{(k)}\boldsymbol{Q}^{(k)}$$
(36)

where the expressions for $\Gamma^{(k)}$ and $Q^{(k)}$ can be deduced from the parent equations. The general conservation equation (36) is integrated over a finite volume (Figure 1b) to yield

$$\iint_{\Omega} \frac{\partial(\alpha^{(k)} \rho^{(k)} \phi^{(k)})}{\partial t} d\Omega + \iint_{\Omega} \nabla \cdot (\alpha^{(k)} \rho^{(k)} \mathbf{u}^{(k)} \phi^{(k)}) d\Omega
= \iint_{\Omega} \nabla \cdot (\alpha^{(k)} \Gamma^{(k)} \nabla \phi^{(k)}) d\Omega + \iint_{\Omega} \alpha^{(k)} Q^{(k)} d\Omega$$
(37)

where Ω is the volume of the control cell. Using the divergence theorem to transform a volume integral into a surface integral, replacing the surface integrals by a summation of the fluxes over the sides of the control volume, and then discretizing

these fluxes using suitable interpolation profiles [29–31], the following algebraic equation results:

$$A_P^{(k)} \phi_P^{(k)} = \sum_{NR} A_{NB}^{(k)} \phi_{NB}^{(k)} + B_P^{(k)}$$
(38)

In compact form, the above equation can be written as

$$\phi_P^{(k)} = H_P[\phi^{(k)}] = \frac{\sum_{NB} A_{NB}^{(k)} \phi_{NB}^{(k)} + B_P^{(k)}}{A_P^{(k)}}$$
(39)

An equation similar to Eq. (38) or (39) is obtained at each grid point in the domain, and the collection of these equations forms a system that is solved iteratively.

The discretization procedure for the momentum equation yields an algebraic equation of the form

$$\mathbf{u}_{P}^{(k)} = \mathbf{H}_{P}[\mathbf{u}^{(k)}] - \alpha^{(k)} \mathbf{D}_{P}^{(k)} \nabla_{P}(P)$$

$$\tag{40}$$

Furthermore, the phasic mass conservation equation can be viewed as a phasic volume fraction equation or as a phasic continuity equation, which can be used in deriving the pressure-correction equation. Its discretized form is given by

$$\frac{(\alpha_P^{(k)} \rho_P^{(k)}) - (\alpha_P^{(k)} \rho_P^{(k)})^{\text{Old}}}{\delta t} \Omega_P + \sum_{f = \text{nb}(P)} \alpha_f^{(k)} \rho_f^{(k)} \mathbf{u}_f^{(k)} \cdot \mathbf{S}_f = B_P^{(k)}$$
(41)

PRESSURE-CORRECTION EQUATION

To derive the pressure-correction equation, the mass conservation equations of the various fluids are added to yield the global mass conservation equation given by

$$\sum_{k} \left\{ \frac{(\alpha_{P}^{(k)} \rho_{P}^{(k)}) - (\alpha_{P}^{(k)} \rho_{P}^{(k)})^{\text{Old}}}{\delta t} \Omega + \sum_{f = \text{nb}(P)} \alpha_{f}^{(k)} \rho_{f}^{(k)} \mathbf{u}_{f}^{(k)} \cdot \mathbf{S}_{f} \right\} = 0$$
 (42)

Denoting the corrections for pressure, density, and velocity by P', $\mathbf{u}^{(k)'}$, and $\rho^{(k)'}$, respectively, the corrected fields are written as

$$P = P^{\circ} + P', \qquad \mathbf{u}^{(k)} = \mathbf{u}^{(k)^*} + \mathbf{u}^{(k)'}, \qquad \rho^{(k)} = \rho^{(k)\circ} + \rho^{(k)'}$$
 (43)

Combining Eqs. (40), (42), and (43), the final form of the pressure-correction equation is obtained as [32]

$$\sum_{k} \left\{ \frac{\Omega}{\delta t} \alpha_{P}^{(k)^{\circ}} C_{\rho}^{(k)} P_{P}' + \sum_{f=\text{nb}(P)} (\alpha^{(k)^{\circ}} U^{(k)^{*}} C_{\rho}^{(k)} P')_{f} - \sum_{f=\text{nb}(P)} [\alpha^{(k)^{\circ}} \rho^{(k)^{*}} (\alpha^{(k)^{\circ}} \mathbf{D}^{(k)} \nabla P') \cdot \mathbf{S}]_{f} \right\}$$

$$= -\sum_{k} \left\{ \frac{\alpha_{P}^{(k)^{\circ}} \rho_{P}^{(k)^{*}} - (\alpha_{P}^{(k)} \rho_{P}^{(k)})^{\text{old}}}{\delta t} \Omega + \sum_{f=\text{nb}(P)} (\alpha^{(k)^{\circ}} \rho^{(k)^{*}} U^{(k)^{*}})_{f} \right\}$$
(44)

The corrections are then applied to the velocity, density, and pressure fields using the following equations:

$$\mathbf{u}_{P}^{(k)*} = \mathbf{u}_{P}^{(k)\circ} - \alpha^{(k)\circ} \mathbf{D}_{P}^{(k)} \nabla_{P} P', \qquad P^{*} = P^{\circ} + P', \qquad \rho^{(k)*} = \rho^{(k)\circ} + C_{\rho}^{(k)} P' \qquad (45)$$

SOLUTION PROCEDURE

The overall solution procedure is an extension of the single-phase SIMPLE algorithm [33, 34] into multiphase flows [32]. The sequence of events in the multiphase algorithm is as follows.

- 1. Solve the fluidic momentum equations for velocities.
- 2. Solve the pressure-correction equation based on global mass conservation.
- 3. Correct velocities, densities, and pressure.
- 4. Solve the fluidic mass conservation equations for volume fractions.
- 5. Solve the fluidic scalar equations $(k, \varepsilon, T, Y, d_d, \text{ etc.})$.
- 6. Return to the first step and repeat until convergence.

NUMERICAL VALIDATION

The above-described solution algorithm is verified by numerically reproducing measurements in an isopropyl alcohol turbulent evaporating spray [35]. Several workers [17, 36] have used this problem to validate their numerical methods.

The experimental setup consists of a cylindrical test section of 194-mm inner diameter into which isopropyl alcohol with a temperature of 313 K is injected from a 20-mm-outer-diameter nozzle located along its axis of symmetry. The co-flowing air is simultaneously blown with a temperature of 373 K through a concentric annulus of 40-mm and 60-mm inner and outer diameters, respectively. The inlet mass flow rates of air and isopropyl alcohol are 28.3 and 0.443 g/s, respectively. Detailed measurements at various axial positions are available for validating the numerical predictions. Radial profiles at x = 3 mm are used to describe the inlet conditions to the domain, while profiles at x = 25, 50, 100, and 200 mm are employed for comparison.

In the numerical solution obtained, the physical domain, considered to be axisymmetric of length 1 m and radius 0.097 m, is discretized using 130×80 nonuniform grids with denser clustering near the nozzle. Droplets are divided according to size into five phases, with the diameter of droplets in the first droplet phase set to $10\,\mu m$ and the increment to $10\,\mu m$ [i.e., droplets of diameters between 10 (droplet phase 1) and $50\,\mu m$ (droplet phase 5) are considered, the range suggested by experimental data [35] within which the bulk of the droplet sizes fall]. The volume fraction profiles of the various phases at the inlet are deduced from available experimental data. The outflow condition is imposed at the exit from the domain, and boundary values are extrapolated from the interior solution. At the walls, a no-slip condition is applied for the momentum equations, while a zero flux condition is used for the volume fraction and mass fraction equations. For the energy equation, the available experimental wall temperature profile is employed.

In Figure 2 comparisons of the numerically predicted radial profiles of the mean axial gas velocity (Figures 2a-2d), the mean axial droplet velocity (averaged

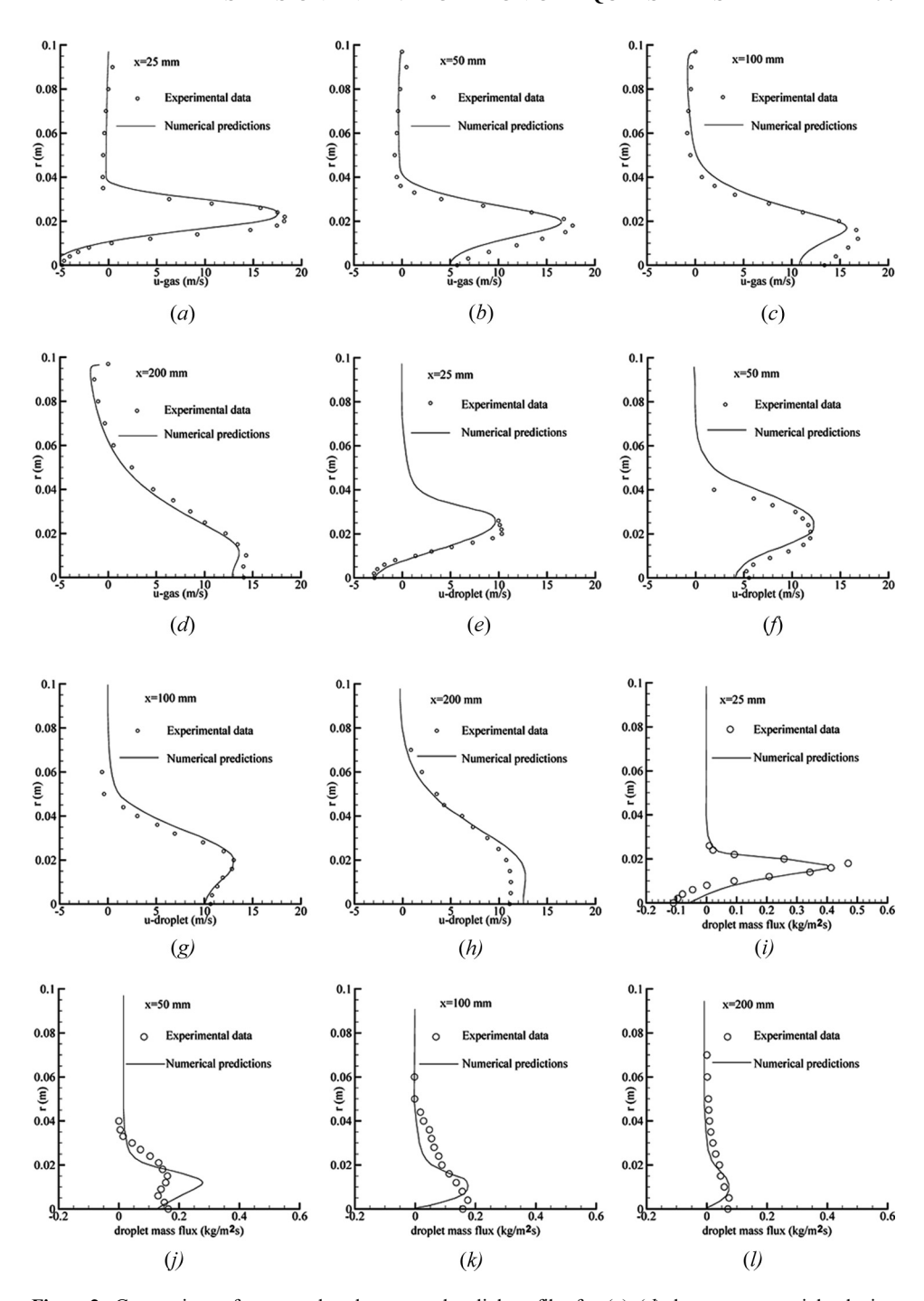


Figure 2. Comparison of measured and computed radial profiles for (a)—(d) the gas mean axial velocity, (e)—(h) the droplet mean axial velocity, and (i)—(l) the liquid-phase mass flow rate.

over the phases, Figures 2e-2h), and liquid mass flux (Figures 2i-2l) against experimental data are presented. As shown, numerical predictions at the four axial locations (x=25, 50, 100, and $200 \, \text{mm}$) are in good agreement with experimental profiles, validating the numerical implementation of the solution algorithm.

RESULTS AND DISCUSSION

The suggested solution algorithm is used to predict, for the configurations depicted in Figures 3a and 3b, mixing and evaporation of droplets in gas streams flowing at subsonic and supersonic speeds. Figure 3a represents a rectangular duct in which air enters with a uniform free-stream velocity U, while kerosene droplets $(C_{12}H_{23}, [37])$ mixed with air are injected through an opening 1 mm in width in the streamwise direction. For the base case, the length of the domain is L (L=1 m) and its width is W (W=0.25 m). Figure 3b differs from Figure 3a in that fuel is sprayed in the cross-stream direction through two openings, located at 10 cm from the duct inlet, each 1 mm wide. For the base case, the length of the domain is L (L=1.1 m) and its width is W (W=0.25 m). An illustrative grid network used is displayed in Figure 3c. For all results presented, five droplet sizes are used of diameters equally spaced and varying between 75 and 150 µm. Therefore all computations were performed using a total of six phases [one gas phase (phase 1) and five droplet phases (phases 2 to 6)]. For all cases presented, the volume fraction values of the droplet phases at inlet are set to $\alpha_{d,\rm in}^{(2)} = 0.1\alpha_{d,\rm in}$, $\alpha_{d,\rm in}^{(3)} = 0.2\alpha_{d,\rm in}$, $\alpha_{d,\rm in}^{(4)} = 0.4\alpha_{d,\rm in}$, $\alpha_{d,\rm in}^{(5)} = 0.1\alpha_{d,\rm in}$, and $\alpha_{d,\rm in}^{(6)} = 0.2\alpha_{d,\rm in}$, where $\alpha_{d,\rm in} = \sum_{k=2}^{6} \alpha_{d,\rm in}^{(k)}$. At the walls, a no-slip

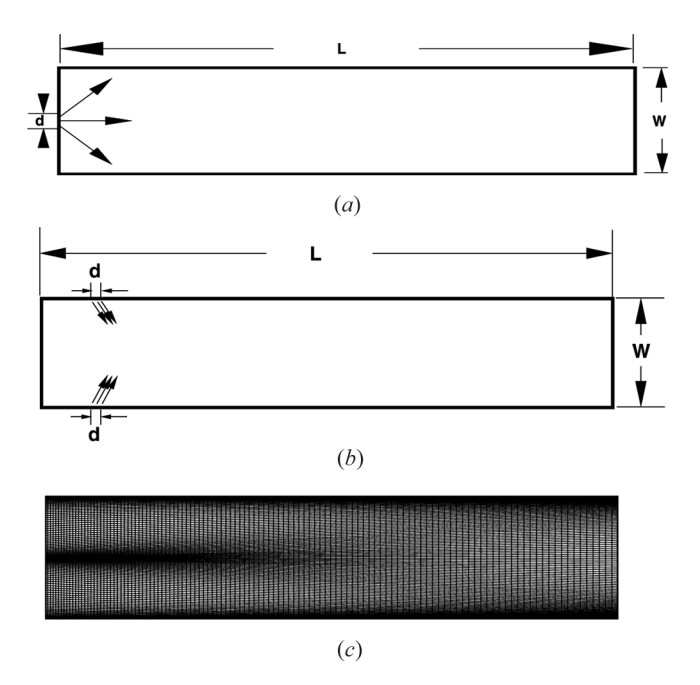


Figure 3. Physical domain for (a) streamwise injection in a rectangular duct, and (b) cross-stream injection in a rectangular duct; (c) an illustrative grid.

condition is applied for the momentum equations, while a zero flux condition is used for the volume fraction, mass fraction, and energy equations. For subsonic flow, values for all variables except pressure are specified at the inlet, while at the exit, pressure is the only variable with a prescribed value. For the supersonic cases, values for all variables are imposed at the inlet to the domain, while values are not set for any variable at the exit section.

To investigate the sensitivity of the solution to the grid used, numerical experiments were carried out with different sizes of nonuniform grids. An example of these experiments involving cross-stream injection in a subsonic flow field is presented in Figure 4. Results displayed in the figure were computed on three grid systems with sizes of 150×104 , 182×104 , and 182×182 cells. The comparisons of the axial gas velocity (Figure 4a), gas temperature (Figure 4b), gas density (Figure 4c), vapor mass fraction (Figure 4d), gas volume fraction (Figure 4e), and gas turbulent kinetic energy (Figure 4f) profiles presented at three axial stations ($x = 0.25 \,\mathrm{m}$, $0.5 \,\mathrm{m}$, and $0.75 \,\mathrm{m}$) and generated using the various grids indicate that they are nearly coinciding. Since the purpose is to test a method, the grid with size of 150×104 cells is selected in subsequent computations involving cross-stream injection. For streamwise injection, a nonuniform grid with size of 132×104 control volumes is used. For both configurations, droplets are injected through 12 uniformly distributed control volumes (each of width $1/12 \,\mathrm{mm}$).

Case 1: Streamwise Injection in a Subsonic Flow Field

For the configuration displayed in Figure 3a, air enters the domain at a Mach number of 0.2 (subsonic flow field) and a temperature of 700 K. Moreover, the kerosene–air mixture is injected with a velocity of magnitude $30 \, \text{m/s}$ at angles varying uniformly between -60° and 60° , a temperature of $400 \, \text{K}$, and a liquid volume fraction of 0.1, resulting in a fuel injection rate of $2.34 \, \text{kg/s/m}$. Results are presented in Figures 5 and 6.

Figure 5 displays the material velocity fields (αu) for the gas phase (Figure 5a) and for droplet phases 1 (75 µm in diameter, Figure 5b), 2 (93.75 µm in diameter, Figure 5c), 3 (112.5 µm in diameter, Figure 5d), 4 (131.25 µm in diameter, Figure 5e), and 5 (150 µm in diameter, Figure 5f). The effect of the spray on the gas field is clearly revealed by the velocity vectors presented in Figure 5a. As shown, a deceleration of the gas phase occurs in the central portion of the domain at the location where the fuel is sprayed. The rate of deceleration decreases in the streamwise direction, but its effect spreads over a wider cross-sectional area due to the dispersion of the injected fuel. Vector fields presented in Figures 5b through 5f reveal a larger droplet spreading (or cross-penetration) with increasing droplet diameter, which is physically correct because larger particles possess higher inertia and are more capable of penetrating into the domain as compared to smaller ones, which align faster with the flow field.

In Figure 6 contour maps of several variables are displayed. The volume fraction of the gas field depicted in Figure 6a indicates that because of the higher air velocity, the spreading of injected fuel is low and droplets quickly align with the air velocity. The distribution of kerosene vapor in the gas phase is displayed in Figure 6b. As shown, the amount of fuel vapor in the gas phase increases as the mixture moves downstream in the channel, due to the increase in the evaporated

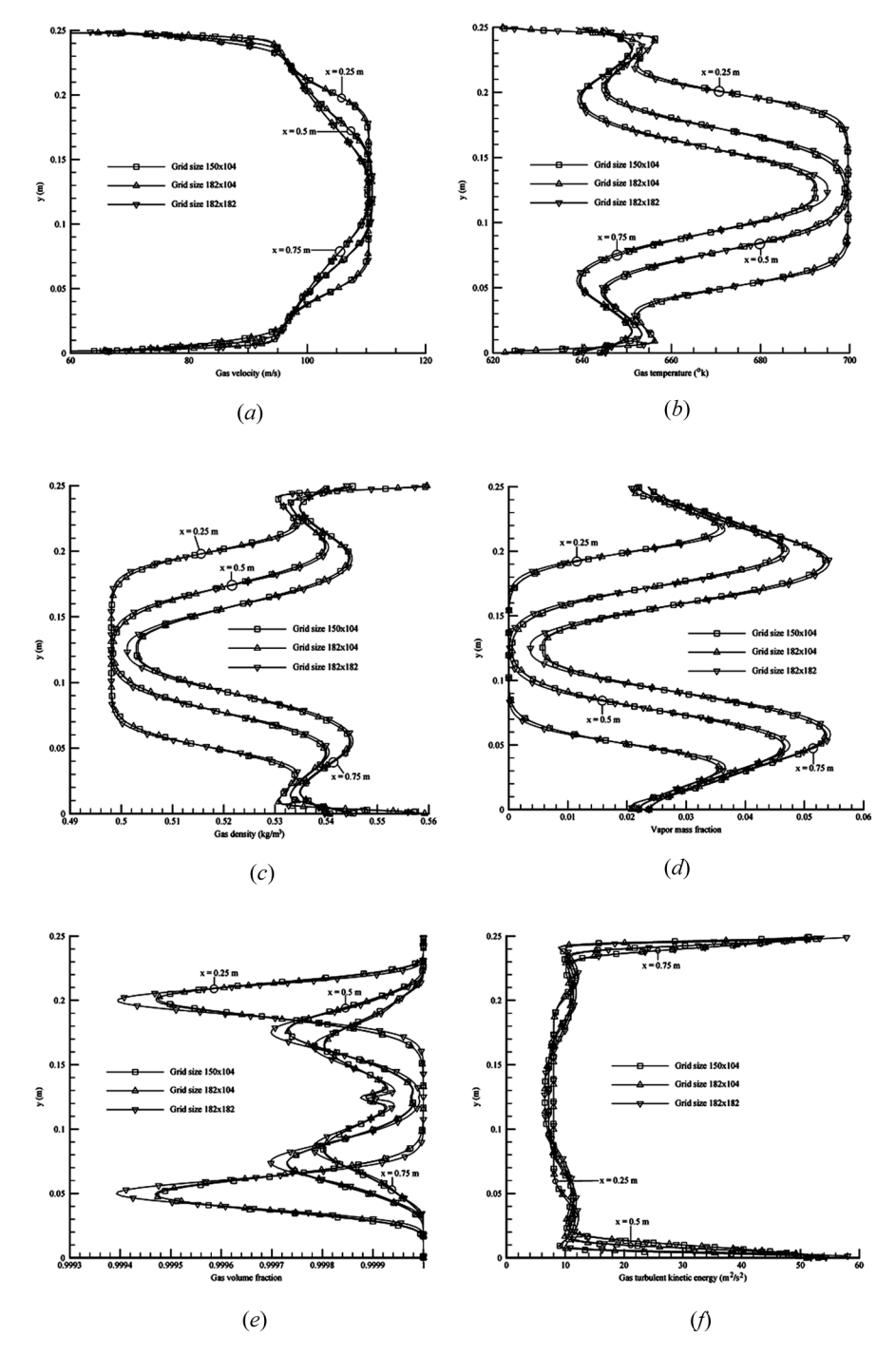


Figure 4. Comparison of the (a) gas u-velocity, (b) gas temperature, (c) gas density, (d) vapor mass fraction, (e) gas volume fraction, and (f) gas turbulent kinetic energy profiles at three axial stations generated using three different grid systems.

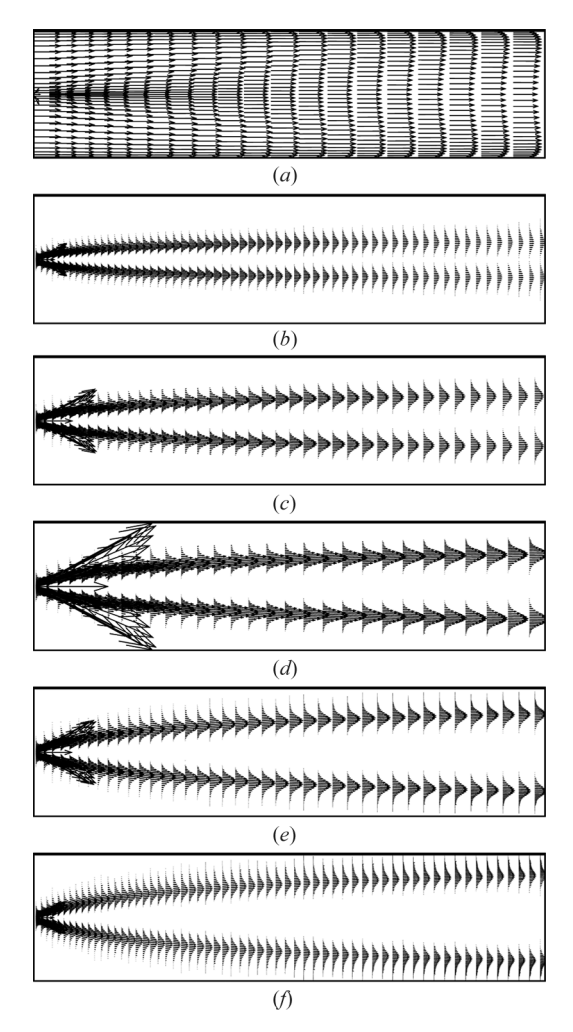


Figure 5. Velocity fields for the gas phase (a) and the droplet phases (b)–(f) in increasing droplet size for streamwise injection in a subsonic flow field ($M_{\rm in}=0.2$).

amount with distance, which is physically plausible. The pressure field is depicted in Figure 6c and indicates larger changes in the spray region where the highest droplet volume fraction exists as a result of the gas-phase deceleration caused by the drag of the injected droplets. As expected, the gas temperature (Figure 6d) decreases in the core region of the domain because of droplet evaporation. The gas turbulent viscosity map shown in Figure 6e indicates that the highest values are in the regions of the domain where the droplets are present and high liquid–gas interaction occurs.

Case 2: Streamwise Injection in a Supersonic Flow Field

For the same physical situation depicted in Figure 3a, the air Mach number is set at 2 (supersonic flow field) and the temperature at 700 K. Moreover, the

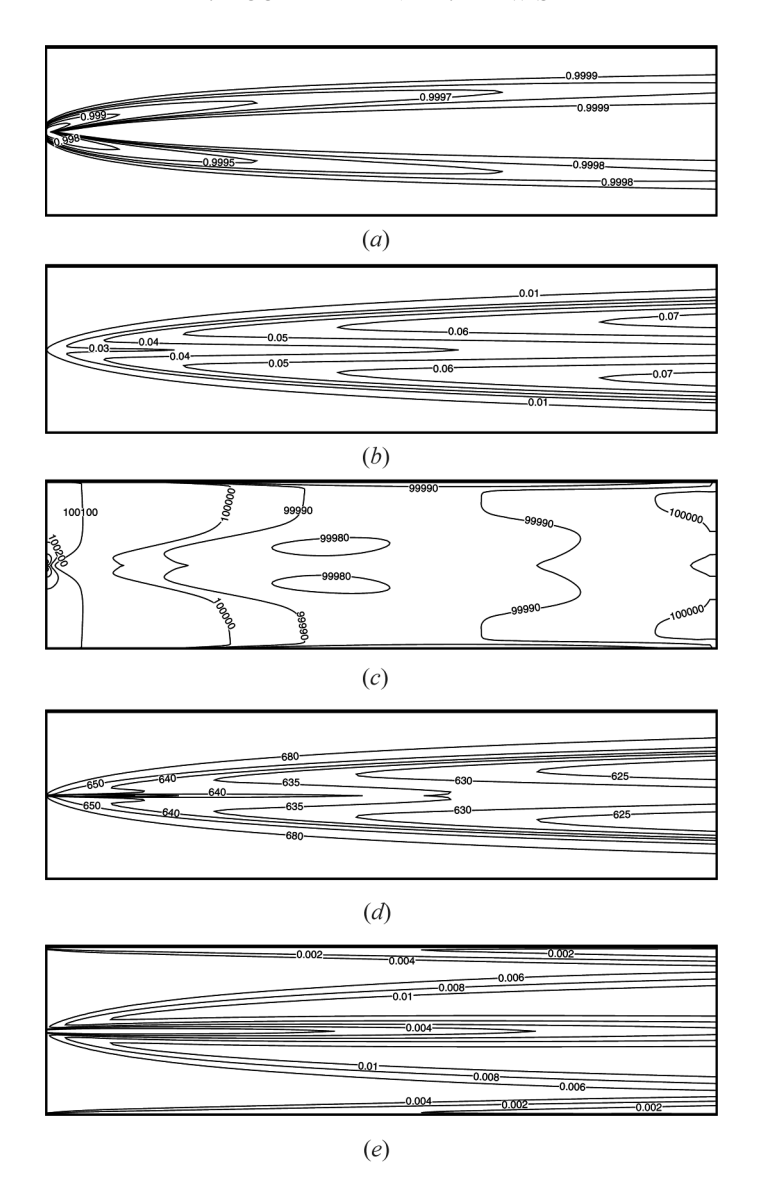


Figure 6. Comparison of (a) gas volume fraction, (b) vapor mass fraction, (c) pressure, (d) gas temperature, and (e) gas turbulent viscosity contours for streamwise injection in a subsonic flow field $(M_{\rm in}=0.2)$.

kerosene–air mixture is injected with a velocity of magnitude $200\,\mathrm{m/s}$ at angles varying uniformly between -60° and 60° , a temperature of $400\,\mathrm{K}$, and a liquid volume fraction of 0.015, resulting in a fuel injection rate of $2.34\,\mathrm{kg/s/m}$. Results generated are presented in Figures 7 and 8.

Figure 7 displays the material velocity fields ($\alpha \mathbf{u}$) for the gas phase (Figure 7a) and for droplet phases 1 through 5 (Figures 7b-7f). The effect of the spray on the gas field (Figure 7a) is similar to the subsonic case (Figure 5a) but it is not as strong because for the same injected amount of fuel, higher velocities are involved, resulting

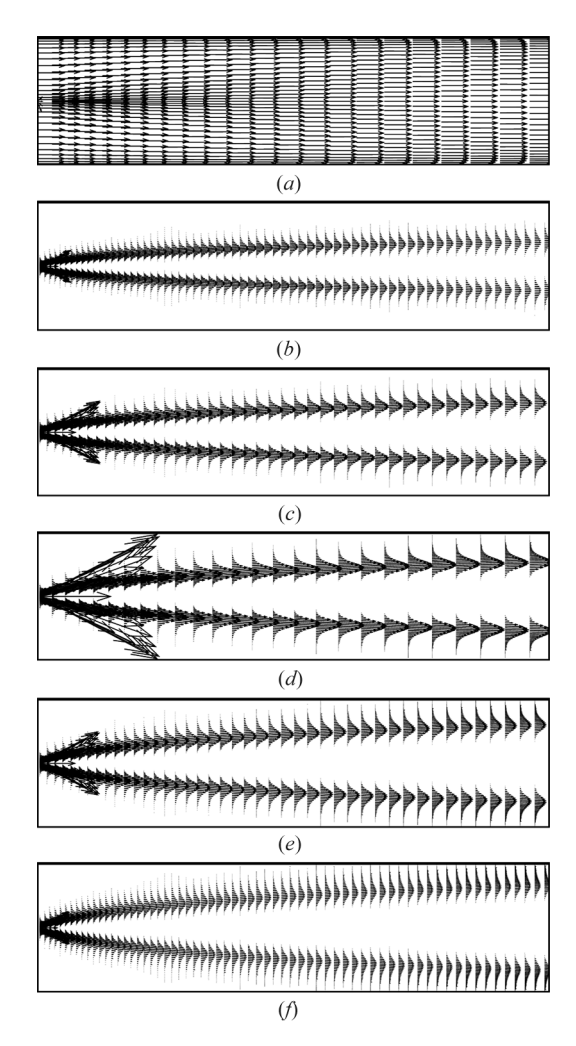


Figure 7. Velocity fields for the gas phase (a) and the droplet phases (b)–(f) in increasing droplet size for streamwise injection in a supersonic flow field $(M_{\rm in}=2)$.

in lower volume fraction values. Droplet velocity vectors reveal that the degree of liquid spreading (cross-penetration) increases with increasing droplet diameter. This is expected, since larger particles possess higher inertia and are more capable of penetrating into the domain. At this supersonic speed, the high degree of droplet penetration obtained is due to the high injection velocity (200 m/s). Droplet velocity fields (not reported here) obtained with low injection velocities in supersonic flow fields resulted in very little spreading of the droplets and remained confined to a narrow region around the centerline of the domain.

In Figure 8, contour maps of the gas volume fraction field (Figure 8a), the fuel vapor in the gas-phase field (Figure 8b), the pressure field (Figure 8c), the gas temperature field (Figure 8d), and the gas turbulent viscosity field (Figure 8e) are presented. The volume fraction of the droplets decreases in the streamwise direction

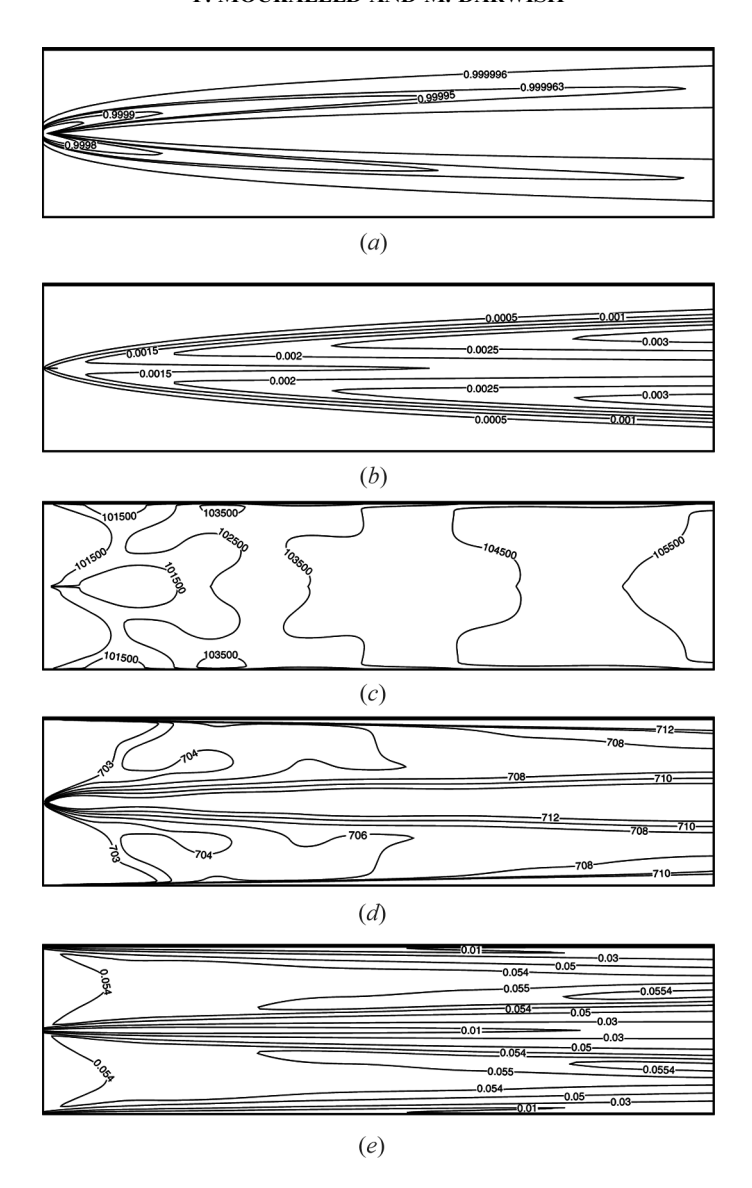


Figure 8. Comparison of (a) gas volume fraction, (b) vapor mass fraction, (c) pressure, (d) gas temperature, and (e) gas turbulent viscosity contours for streamwise injection in a supersonic flow field $(M_{\rm in}=2)$.

(i.e., an increase in the gas volume fraction is obtained), while the mass fraction of the fuel vapor in the gas phase increases in the streamwise direction as more kerosene evaporates. To be noticed is the increase in pressure values in the streamwise direction due to the decrease in the flow velocity caused by drag. At supersonic speeds the decrease in velocity, the turbulent fluctuations, and the viscous dissipation increase the gas temperature. This statement can be clarified by considering the decrease in velocity of the gas phase as an example. Numerical results reveal a decrease in the

gas-phase velocity from nearly 1,060 m/s to 1,035 m/s over a few control volumes close to the nozzle. This decrease in velocity alone causes the gas temperature to increase by about 26°C, which supports the previously stated statement. On the other hand, droplet evaporation decreases the gas temperature. The relative strength of these factors dictates the gas temperature distribution over the domain, which is seen to increase slightly over the inlet value in this case. Finally, the largest gas turbulent viscosity values occur along the droplet trajectories, because of liquid—gas interactions.

Case 3: Cross-Stream Injection in a Subsonic Flow Field

For the configuration displayed in Figure 3b, air enters the domain at a Mach number of 0.2 (subsonic flow field) and a temperature of 700 K. Moreover, the kerosene–air mixture is injected with a velocity of magnitude $30 \,\mathrm{m/s}$ at an angle of 30° to the direction of the gas flow, a temperature of $400 \,\mathrm{K}$, and a liquid volume fraction of 0.08, resulting in a total fuel injection rate, from both nozzles, of $1.872 \,\mathrm{kg/s/m}$.

Results obtained using the above-described solution procedures are presented in Figures 9 and 10. Figures 9a-9e display the material velocity fields ($\alpha \mathbf{u}$) for the gas and droplet phases. The effect of the spray on the gas field can be inferred from the velocity vectors presented in Figure 9a. This effect is seen to be strong in the region close to the injector and to weaken as the sprayed jet scatters. Moreover, droplet velocity vectors presented in Figures 9b-9f indicate larger droplet spreading (or cross-penetration) with increasing droplet diameter, with the smallest droplets flowing close to the walls and the largest droplets penetrating into the core of the domain, which is physically correct.

In Figure 10, contours of the gas volume fraction field (Figure 10a), the fuel vapor field in the gas phase (Figure 10b), the pressure field (Figure 10c), the gas temperature field (Figure 10d), and the gas turbulent viscosity field (Figure 10e) are presented. As depicted, variations in these quantities are similar to those reported in Figure 6, with the gas volume fraction field mimicking the droplet velocity fields, the fuel vapor in the gas phase increasing in the streamwise direction as more liquid evaporates, the largest variation in pressure occurring in the spray region, the gas temperature decreasing as evaporation takes place, and the gas turbulent viscosity maximizing along the droplet trajectories where high liquid—gas interaction occurs.

Case 4: Cross-Stream Injection in a Supersonic Flow Field

For the same configuration depicted in Figure 3b, the air Mach number is set at 2 (supersonic flow field) and the temperature at 700 K. Moreover, the kerosene–air mixture is injected with a velocity of magnitude $200\,\mathrm{m/s}$ at an angle of 30° to the direction of the gas flow, a temperature of $400\,\mathrm{K}$, and a liquid volume fraction of 0.012, resulting in a total fuel injection rate, from both nozzles, of $1.872\,\mathrm{kg/s/m}$. Generated results are displayed in Figures 11 and 12.

Due to the lower volume fractions involved, the effect of the spray on the supersonic gas phase (Figure 11a) is weaker than in the subsonic case. However, the droplet material velocity vectors displayed in Figure 11 indicate similar behavior

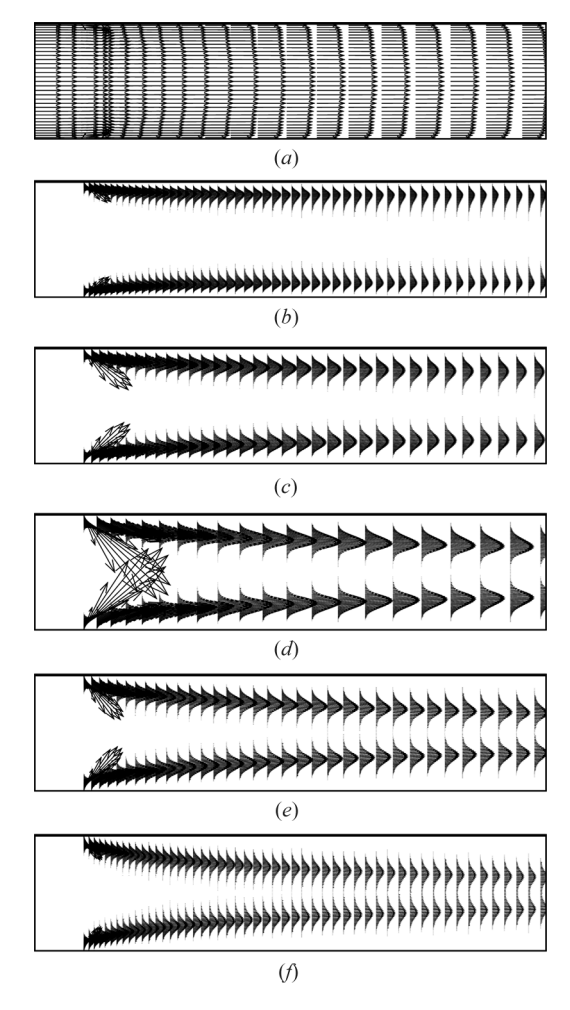


Figure 9. Velocity fields for the gas phase (a) and the droplet phases (b)–(f) in increasing droplet size for cross-stream injection in a subsonic flow field ($M_{\rm in} = 0.2$).

to the cases presented earlier with larger particles penetrating deeper into the inner domain (compare Figures 11*b*–11*f* for phases 1–5, with phase 5 having the largest droplet diameter).

In Figure 12, contour maps of the volume fraction field (Figure 12a), the fuel vapor in the gas-phase field (Figure 12b), the pressure field (Figure 12c), the gas temperature field (Figure 12d), and the gas turbulent viscosity field (Figure 12e) are presented. The general trend in the variation of these variables resembles that presented in case 2, i.e., the volume fraction of the particles decreases in the streamwise direction, the mass fraction of the liquid vapor in the gas phase increases in the streamwise direction with the largest variations occurring close to the nozzle exits, the gas temperature increases slightly for the same reasons stated earlier, and the largest gas turbulent viscosity values occurs at locations where high fuel—air mixing occurs.

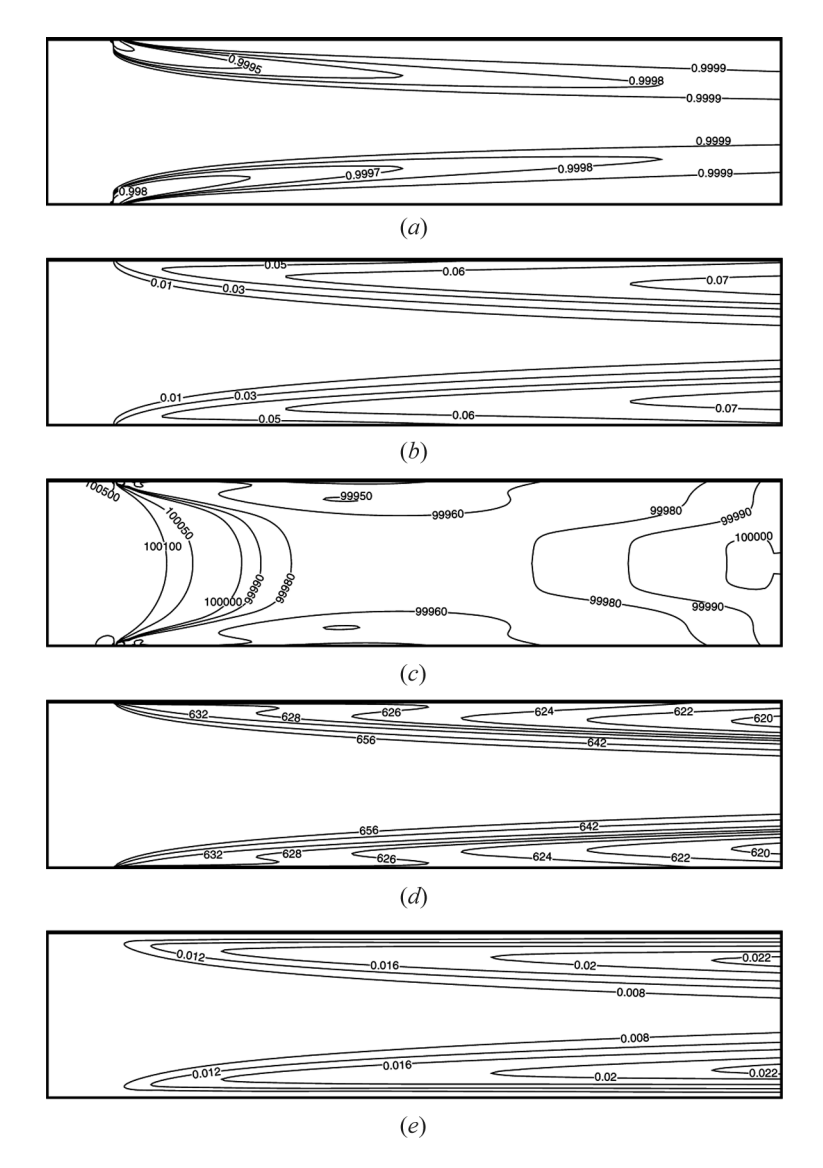


Figure 10. Comparison of (a) gas volume fraction, (b) vapor mass fraction, (c) pressure, (d) gas temperature, and (e) gas turbulent viscosity contours for cross-stream injection in a subsonic flow field ($M_{\rm in}=0.2$).

Parametric Study

A parametric study was also undertaken to investigate the effects of varying the inlet gas temperature, inlet droplet temperature, and duct length on the percentage of the injected fuel that evaporates into the gas phase in all configurations, and results are displayed in Figure 13. In generating results, only the parameter under investigation is varied in the range shown on the plot and, depending on the case, the remaining parameters are assigned the values presented earlier.

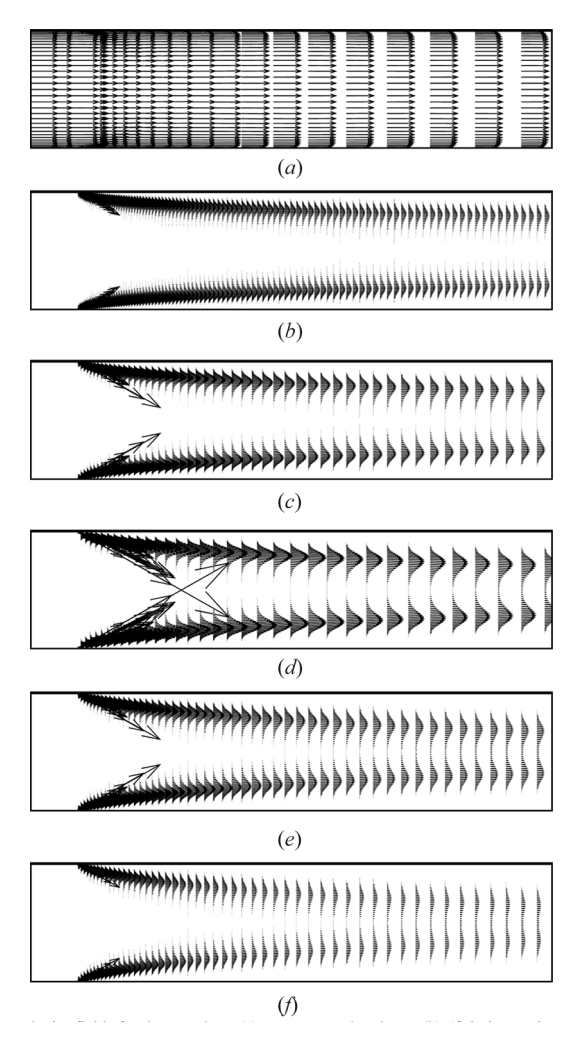


Figure 11. Velocity fields for the gas phase (a) and the droplet phases (b)–(f) in increasing droplet size for cross-stream injection in a supersonic flow field ($M_{\rm in} = 2$).

As expected, the amount of evaporating liquid increases with increasing inlet gas temperature (Figure 13a), increasing inlet droplet temperature (Figure 13b), and increasing channel length (Figure 13c). Moreover, it can be inferred from Figures 13a–13c that the fraction that evaporates decreases as the gas velocity increases. Furthermore, the difference in the evaporating fractions between streamwise and cross-stream injection is insignificant at subsonic speed, with the percentage being marginally higher for cross-stream injection. The same trend is noticed at supersonic speeds, with the difference being larger. The higher evaporating percentages at supersonic speeds for cross-stream injection are attributed to the increase in temperature close to the wall, which enhances evaporation.

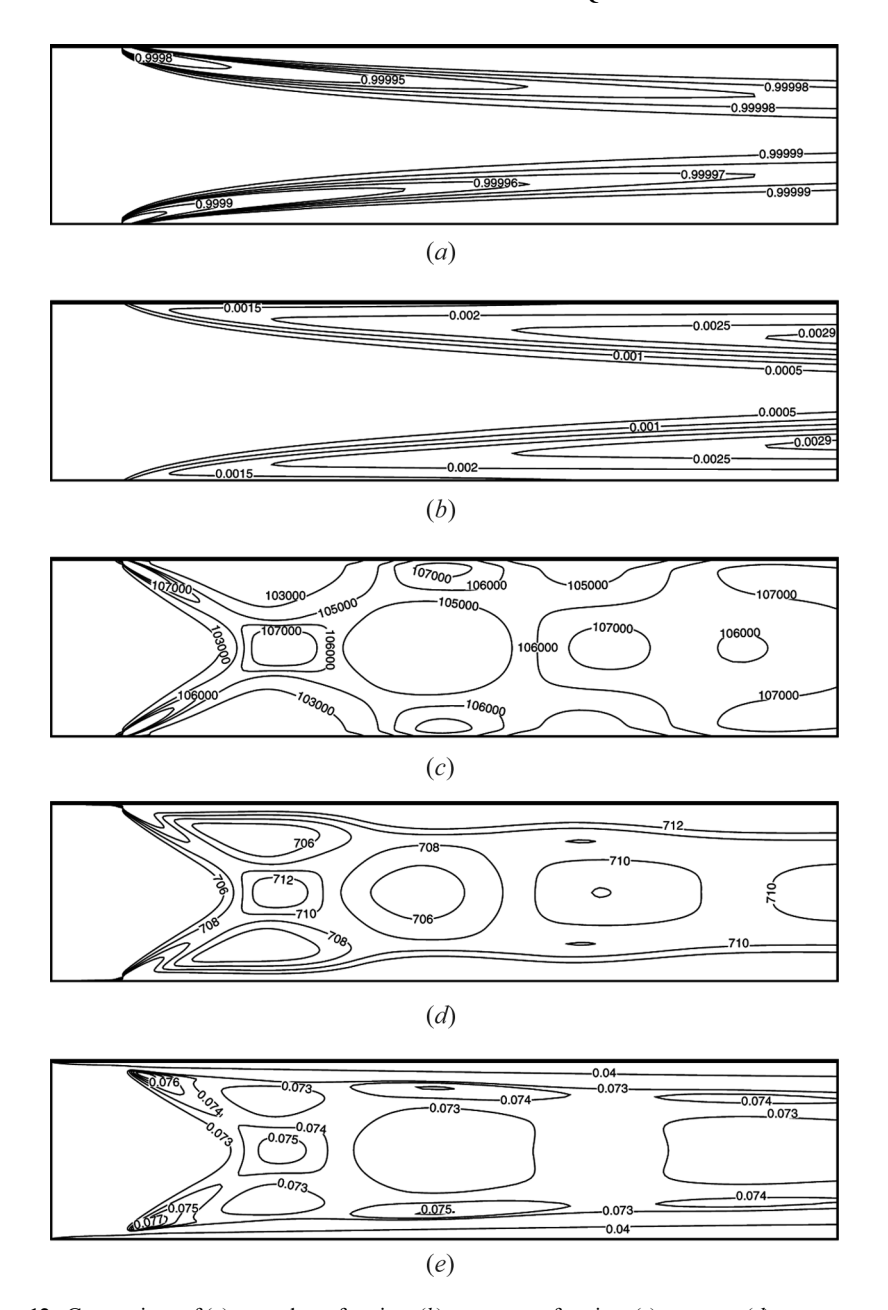


Figure 12. Comparison of (a) gas volume fraction, (b) vapor mass fraction, (c) pressure, (d) gas temperature, and (e) gas turbulent viscosity contours for cross-stream injection in a supersonic flow field ($M_{\rm in}=2$).

CLOSING REMARKS

A Eulerian model involving discrete and continuous phases for the simulation of droplet evaporation and mixing at all speeds was formulated and implemented.

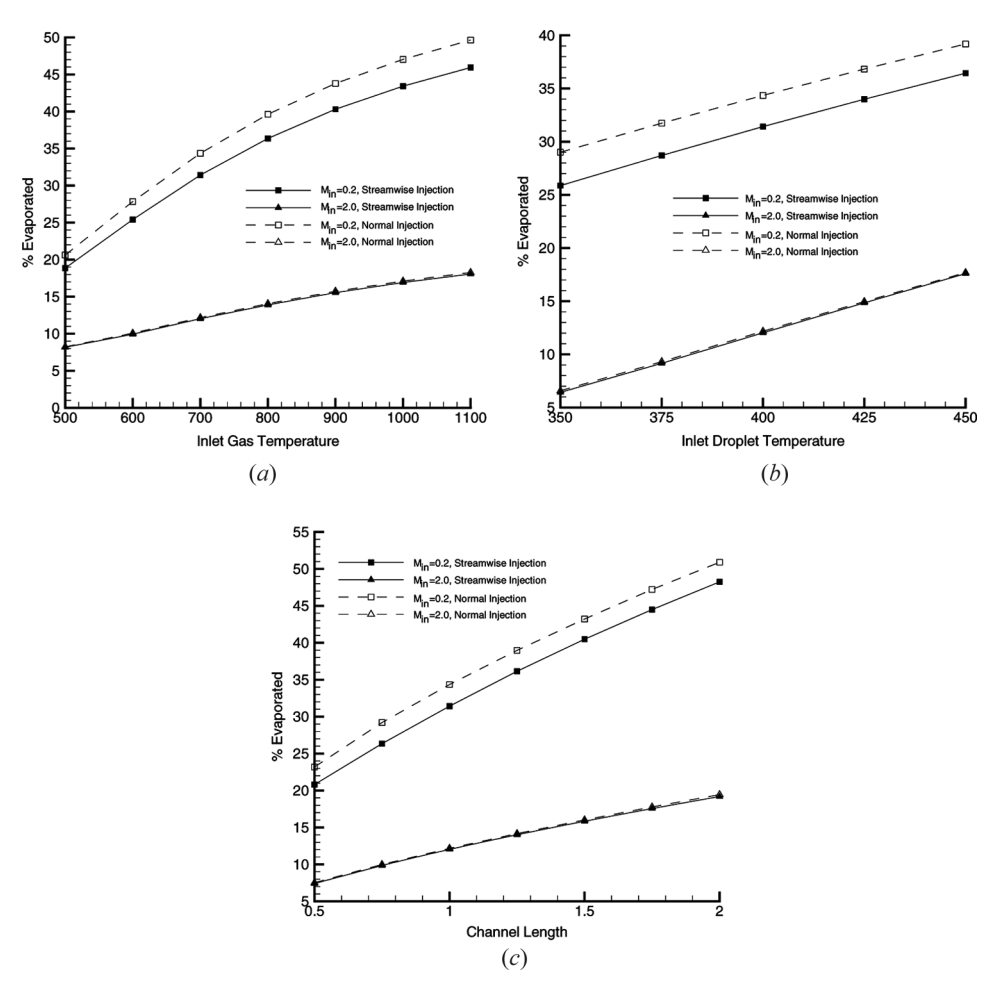


Figure 13. Comparison of evaporation rate for the various configurations as a function of; (a) inlet gas temperature; (b) inlet droplet temperature; (c) channel length.

The model allows for continuous droplet size changes without recourse to a stochastic approach. The numerical procedures follow on a pressure-based multifluid finite-volume method and form a solid base for the future inclusion of other modes of interactions such as droplet coalescence and breakup. Turbulence was modeled using the two-equation $k-\varepsilon$ turbulence model for the continuous gas phase, with modifications to account for gas compressibility at high speeds, coupled with an algebraic model for the discrete phase. The method was tested by solving for evaporation and mixing in two physical configurations involving streamwise and cross-stream injections, in the subsonic and supersonic regimes, over a wide range of operating conditions. Reported results indicated an increase in the rate of evaporation with increasing inlet gas temperature, inlet droplet temperature, and/or length of the domain, which is physically correct.

REFERENCES

- 1. D. W. Bogdanoff, Advanced Injection and Mixing Techniques for Scramjet Combustors, J. Propulsion Power, vol. 10, pp. 183–190, 1994.
- 2. I. W. Kay, W. T. Peshke, and R. N. Guile, Hydrocarbon Fueled Scramjet Combustor Investigations, *J. Propulsion Power*, vol. 8, pp. 507–512, 1992.
- 3. A. Rajasekaran and V. Babu, Numerical Simulation of Kerosene Combustion in a Dual Mode Supersonic Combustor, 42nd AIAA/ASME/SAE/ASEE Joint Propulsion Conference and Exhibition, Sacremento, CA, 9–12 July 2006, Paper AIAA-2006-5041.
- 4. C. Lee, K. Lee, J. Senda, and H. Fujimoto, A Study on the Spray-Wall Interaction Model Considering Degree of Superheat in the Wall Surface, *Numer. Heat Transfer B*, vol. 40, pp. 495–513, 2001.
- 5. M. Burger, G. Klose, G. Rottenkolber, R. Schmehl, D. Giebert, O. Schafer, R. Koch, and S. Wittig, A Combined Eulerian and Lagrangian Method for Prediction of Evaporating Sprays, *J. Eng. Gas Turbines Power*, vol. 124, pp. 481–488, 2002.
- R. Schmehl, G. Klose, G. Maier, and S. Wittig, Efficient Numerical Calculation of Evaporating Sprays in Combustion Chamber Flows, 92nd Symp. on Gas Turbine Combustion, Emissions and Alternative Fuels, RTO Meeting Proceedings 14, 1998.
- 7. M. Hallmann, M. Scheurlen, and S. Wittig, Computation of Turbulent Evaporating Sprays: Eulerian versus Lagrangian Approach, *J. Eng. Gas Turbines Power*, vol. 117, pp.112–119, 1995.
- 8. S. Wittig, M. Hallmann, M. Scheurlen, and R. Schmehl, A New Eulerian Model for Turbulent Evaporating Sprays in Recirculating Flows, *AGARD*, *Fuels and Combustion Technology for Advanced Aircraft Engines*, SEE N94-29246 08-25, May 1993.
- 9. G. Klose, R. Schmehl, R. Meier, G. Maier, R. Koch, S. Wittig, M. Hettel, W., Leuckel, and N. Zarzalis, Evaluation of Advanced Two-Phase Flow and Combustion Models for Predicting Low Emission Combustors, *J. Eng. Gas Turbines Power*, vol. 123, pp. 817–823, 2001.
- 10. F. Nmira, A. Kaiss, J.-L. Consalvi, and B. Porterie, Predicting Fire Suppression Efficiency Using Polydisperse Water Sprays, *Numer. Heat Transfer A*, vol. 53, pp. 132–156, 2008.
- 11. M. S. Raju, On the Importance of Chemistry/Turbulence Interactions in Spray Computations, *Numer. Heat Transfer B*, vol. 41, pp. 409–432, 2002.
- 12. W. K. Chow and B. Yao, Numerical Modeling for Interaction of a Water Spray with Smoke Layer, *Numer. Heat Transfer A*, vol. 39, pp. 267–283, 2001.
- 13. A. K. Tolpadi, S. K. Aggarwal, and H. C. Mongia, An Advanced Spray Model for Application to the Prediction of Gas Turbine Combustor Flow Fields, *Numer. Heat Transfer A*, vol. 38, pp. 325–340, 2000.
- 14. Y. M. Kim, S. J. Kim, Z. J. Chen, and C. P. Chen, Numerical Simulation of Combustion Wave Propagation in an Air-Fuel Spray Mixture with Temperature Nonuniformity, *Numer. Heat Transfer A*, vol. 34, pp. 23–41, 1998.
- 15. M. S. Raju, Application of Scalar Monte Carlo Probability Density Function Method for Turbulent Spray Flames, *Numer. Heat Transfer A*, vol. 30, pp. 753–777, 1996.
- 16. Z. Liu and R. D. Reitz, Modeling Fuel Spray Impingement and Heat Transfer between Spray and Wall in Direct Injection Diesel Engines, *Numer. Heat Transfer A*, vol. 28, pp. 515–529, 1995.
- 17. X.-Q. Chen and J. C. F. Pereira, Prediction of Evaporating Spray in Anisotropically Turbulent Gas Flow, *Numer. Heat Transfer A*, vol. 27, pp. 143–162, 1995.
- 18. M. Jicha, K. C. Karki, and S. V. Patankar, Numerical Analysis of Water Spray System in the Entrance Region of a Two-Dimensional Channel Using Lagrangian Approach, *Numer. Heat Transfer A*, vol. 26, pp. 1–16, 1994.

- 19. B. E. Launder and D. B. Spalding, The Numerical Computation of Turbulent Flows, *Comput. Meth. Appl. Mech. Eng.*, vol. 3, pp. 269–289, 1974.
- 20. B. E. Launder and B. I. Sharma, Application of the Energy Dissipation Model of Turbulence to the Calculation of the Flow near a Spinning Disk, *Lett. Heat Mass Transfer*, vol. 1, pp. 131–137, 1974.
- 21. G. M. Faeth, Evaporation and Combustion of Sprays, *Prog. Energy Combustion Science*, vol. 9, pp. 1–76, 1983.
- 22. S. K. Aggarwal and F. Peng, A Review of Droplet Dynamics and Vaporization Modeling for Engineering Calculations, *J. Eng. Gas Turbines Power*, vol. 117, pp. 453–461, 1995.
- 23. W. A. Sirignano, Fuel Droplet Vaporization and Spray Combustion Theory, *Prog. Energy Combustion Sci.*, vol. 9, pp. 291–322, 1984.
- 24. N. Frössling, Über die Verdunstung fallender Tropfen, *Gerlands Beiträge zur Geophysik*, vol. 52, pp. 170–215, 1938.
- 25. B. Abramzon and W. A. Sirignamo, Droplet Vaporization Models for Spray Combustion Calculations, *Int. J. Heat Mass Transfer*, vol. 32, pp.1605–1618, 1989.
- F. M. Sparrow and J. L. Gregg, The Variable Fluid Property Problem in Free Convection, Trans. ASME, vol. 80, pp. 879–886, 1958.
- 27. W. K. Melville and K. N. C. Bray, A Model of the Two Phase Turbulent Jet, *Int. J. Heat Mass Transfer*, vol. 22, pp. 647–656, 1979.
- 28. M. Krämer, Untersuchungen zum Bewegungsverhalten von Tropfen in turbulenter Strömung im Hinblick auf Verbrennungsvorgänge, Dissertation, Institut für Feuerungstechnik, Universität Karlsruhe (T.H.), 1988.
- 29. P. J. Zwart, G. D. Raithby, and M. J. Raw, An Integrated Space-Time Finite-Volume Method for Moving-Boundary Problems, *Numer. Heat Transfer B*, vol. 34, pp. 257–270, 1998.
- 30. P. H. Gaskell and A. K. C. Lau, Curvature Compensated Convective Transport: SMART, a New Boundedness Preserving Transport Algorithm, *Int. J. Numer. Meth. Fluids*, vol. 8, pp. 617–641, 1988.
- 31. M. S. Darwish and F. Moukalled, Normalized Variable and Space Formulation Methodology for High-Resolution Schemes, *Numer. Heat Transfer B*, vol. 26, pp. 79–96, 1994.
- 32. M. Darwish, F. Moukalled, and B. Sekar, A Unified Formulation of the Segregated Class of Algorithms for Multi-fluid Flow at All Speeds, *Numer. Heat Transfer B*, vol. 40, pp. 99–137, 2001.
- 33. S. V. Patankar, Numerical Heat Transfer and Fluid Flow, Hemisphere, New York, 1981.
- F. Moukalled and M. Darwish, A Unified Formulation of the Segregated Class of Algorithms for Fluid Flow at All Speeds, *Numer. Heat Transfer B*, vol. 37, pp. 103–139, 2000.
- 35. M. Sommerfeld and H. Qiu, Experimental Studies of Spray Evaporation in Turbulent Flow, *Int. J. Heat Fluid Flow*, vol. 19, pp. 10–22, 1998.
- 36. M. A. Founti, D. I. Katsourinis, and D. I. Kolaitis, Turbulent Sprays Evaporating under Stabilized Cool Flame Conditions: Assessment of Two CFD Approaches, *Numer. Heat Transfer B*, vol. 52, pp. 51–68, 2007.
- 37. Fluent database, Release 6.3.26, Fluent, Inc., 2006.